AIAA JOURNAL
Vol. 30, No. 8, August 1992

# Postbuckling Response and Failure Prediction of Graphite-Epoxy Plates Loaded in Compression

S. P. Engelstad* and J. N. Reddy†
*Virginia Polytechnic Institute and State University, Blacksburg, Virginia 24061*
and
N. F. Knight Jr.‡
*Clemson University, Clemson, South Carolina 29634*

**The objective of the study is to predict the postbuckling response and failure modes of various graphite-epoxy panels loaded in axial compression. A shear deformable (three-dimensional) shell element is used to analyze the panels. Two panels without holes and one with a hole are studied, and the resulting responses and failure modes correlated well with the experimental results. A progressive damage failure mechanism is applied in the nonlinear analysis, which proved successful in predictions of failure location, mode, and load.**

## Introduction

USE of composite materials in aircraft and space structures has led to increased research activity in structural modeling, postbuckling response determination, and failure mode characterization of structures made from these materials. Whereas composite materials offer many desirable structural properties over conventional materials, they also pose challenging technical problems in understanding their structural response and failure characteristics. Classical lamination theory, in which the transverse shear effects are neglected, is often used to analyze laminated composite structures. Because of low transverse moduli and strengths relative to in-plane moduli and strengths, composite laminates may fail due to transverse stresses. Therefore, shear deformation plate and shell theories and associated finite element formulations are needed to provide information regarding the transverse shear strength of composite structures. Various shear deformation theories and their computational models have been summarized in Refs. 1–3. Insight gained by using these formulations may aid in the characterization of failure modes of composite panels.

The objectives of this paper are to investigate, using shear-deformable finite elements, the postbuckling response of several graphite-epoxy panels loaded in axial compression and to substantiate analytically the failure modes observed during testing. Comparisons between the experimentally obtained and analytically determined postbuckling response of these composite panels are made.

## Experimental Study

The postbuckling and failure characteristics of flat, rectangular graphite-epoxy panels with and without holes and loaded in axial compression have been examined in an experimental study by Starnes and Rouse.[4] The panels were fabricated from commercially available unidirectional Thornel 300 graphite-fiber tapes preimpregnated with 450 K cure Narmco 5208 thermosetting epoxy resin.§ Typical lamina properties for this graphite-epoxy system are 131.0 GPa (19,000 ksi) for the longitudinal Young's modulus, 13.0 GPa (1,890 ksi) for the transverse Young's modulus, 6.4 GPa (930 ksi) for the in-plane and transverse shear moduli ($G_{12}$ and $G_{13}$), 1.7 GPa (250 ksi) for the other transverse shear modulus ($G_{23}$), 0.38 for the major Poisson's ratio ($\nu_{12}$), and 0.14 mm (0.0055 in.) for the lamina thickness. Each panel was loaded in axial compression using a 1.33-MN (300-kips) capacity hydraulic testing machine. The loaded ends of the panel were clamped by fixtures during testing, and the unloaded edges were simply supported by knife-edge restraints to prevent the panels from buckling as wide columns. A typical panel mounted in the support fixture is shown in Fig. 1a. Most panels exhibited postbuckling strength and failed along a nodal line of the buckling mode in a transverse shear failure mode, as shown in Fig. 1b. However, a failure mode different from this failure mode was observed for some of the 24-ply panels with holes. These panels failed along a transverse line passing through the hole and failed soon after buckling. Information from moire-fringe patterns of transverse displacement was used to assist in determining the failure modes of all panels. No photomicrographs on delamination failures were reported in Ref. 4.

In this paper, three panels from Ref. 4 are analyzed, and the analytical results are compared with the experimental results presented in Ref. 4. The first panel is the 50.8-cm-long × 17.8-cm-wide (20.0-in.-long × 7.0-in.-wide) 24-ply orthotropic laminate with a $[\pm 45/0_2\ \pm 45/0_2\ \pm 45/0/90]_s$ stacking sequence, denoted as panel C4 in Ref. 4. Panel C4 was observed in the test to buckle into two longitudinal half-waves and one transverse half-wave. The second panel is the 50.8-cm-long × 14.0-cm-wide (20.0-in.-long × 5.5-in.-wide) 24-ply quasi-isotropic laminate with a $[\pm 45/0/90]_{3s}$ stacking sequence, denoted as panel C10 in Ref. 4. Panel C10 was observed in the test to buckle into four longitudinal half-waves and one transverse half-wave. The third panel, denoted panel H4 in Ref. 4, is identical to panel C10 except for a 1.91-cm-diam (0.75-in.-diam) hole located 19.1 cm (7.5 in.) from one

---

Received March 19, 1991; presented as Paper 91-0910 at the AIAA/ASME/AHS/ASC 32nd Structures, Structural Dynamics, and Materials Conference, Baltimore, MD, April 8–10, 1991; revision received Jan. 25, 1992; accepted for publication Jan. 25, 1992.

*Assistant Professor, Department of Engineering Science and Mechanics; currently at Lockheed Aeronautical Systems Co., Marietta, GA 30063.

†Clifton C. Garvin Professor, Department of Engineering Science and Mechanics; currently, Oscar S. Waytt Chair, Department of Mechanical Engineering, Texas A&M University, College Station, TX 77843.

‡Associate Professor, Department of Mechanical Engineering. Senior Member AIAA.

§Identification of commercial products and companies in this paper is used to describe adequately the test materials. The identification of these commercial products does not constitute endorsement, expressed or implied, of such products by Virginia Polytechnic Institute and State University, Clemson University, or the publisher of these proceedings.

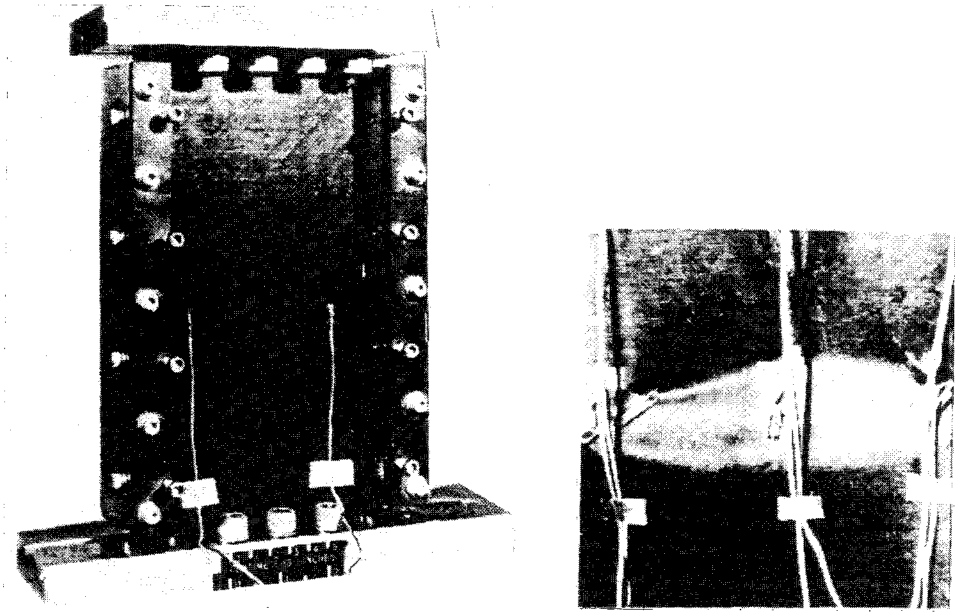

a) Typical panel with fixture b) Failure mode

**Fig. 1 Flat, rectangular graphite-epoxy panel (from Ref. 4).**

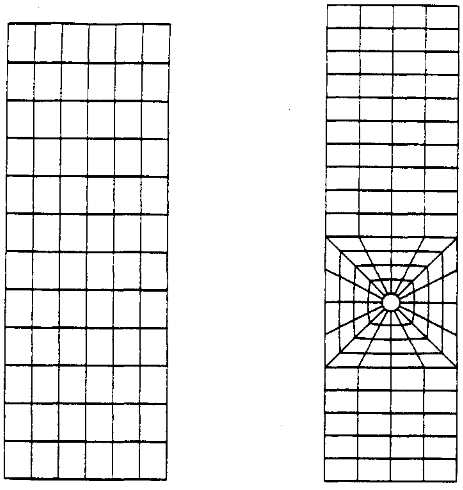

a) C4 specimen model b) H4 specimen model

**Fig. 2 Finite element discretizations.**

of the loaded edges and along the panel centerline. Panel H4 was observed in the test to buckle into four longitudinal half-waves and one transverse half-wave with the hole located near the buckle crest of the second longitudinal half-wave.

Finite element models of these panels were developed using nine-node quadrilateral shell elements. The element formulation is that of a continuum-based theory that leads to three-dimensional degenerated shell elements. The element implementation considered in this study is the Chao-Reddy nine-node (9CR) element.[5] The modeling approach is based on using six elements per buckle half-wave in each direction. Hence, the finite element model of panel C4 has 12 elements along the panel length, whereas that of panel C10 has 24 elements along the panel length. Both panels have six elements across the panel width. Figure 2a shows the model used for the C4 specimen. The finite element model of panel H4 is different due to the presence of the hole. This finite element model has four rings of elements around the hole with each ring subdivided into 16 elements, as shown in Fig. 2b. The total number of nine-node quadrilateral elements in the finite element models of panels C4, C10, and H4 are 72, 144, and 124, respectively. Other finite element discretizations were also considered to verify the modeling approach and were discussed in Ref. 6.

In order to efficiently proceed beyond the critical buckling point in the analysis of each panel, an initial geometric imperfection was assumed, typically the same shape as the first linear buckling mode. The amplitude of each mode was selected to be 1-5% of the total laminate thickness. In this way, an eccentricity is added to the initial geometry that allows efficient progress past the critical buckling point, but does not affect the results in the postbuckling range.

## Degenerated Shell Element Formulation

The incremental equations of a continuous medium are formulated based on the principle of virtual displacements and the total Lagrangian description. The detailed description can be found in Ref. 5 and is omitted here for brevity. The final incremental equilibrium equations for an element are given by

$$([K_L] + [K_{\mathrm{NL}}])\{\Delta\} = \{R\} - \{F\} \tag{1}$$

where $\{\Delta\}$ is the vector of nodal incremental displacements in an element, and $[K_L]$, $[K_{\mathrm{NL}}]$, and $\{F\}$ are obtained from the following integrals, respectively,

$$[K_L] = \int_V [B_L]^T[C][B_L]\,\mathrm{d}V$$

$$[K_{\mathrm{NL}}] = \int_V [B_{\mathrm{NL}}][C][B_{\mathrm{NL}}]\,\mathrm{d}V$$

$$\{F\} = \int_V [B_L]\{\hat{S}\}\,\mathrm{d}V$$

In these equations, $[B_L]$ and $[B_{\mathrm{NL}}]$ are linear and nonlinear strain-displacement transformation matrices, respectively. $[C]$ is the incremental stress-strain material property matrix, $\{\hat{S}\}$ a vector of second-Piola-Kirchhoff stresses, and $\{R\}$ the external load vector. All matrix elements refer to the deformed state and are measured with respect to the original undeformed configuration.

After assembly, the following linearized versions of the actual equilibrium equations are obtained

$$[\hat{K}]\{\Delta\} = \{\hat{R}\} \tag{2}$$

where

$$[\hat{K}] = [K_L] + [K_{\mathrm{NL}}]$$

$$[\hat{R}] = \{R\} - \{F\}$$

The Newton-Raphson method is employed to solve the linearized equations iteratively until the actual equations of equilibrium are satisfied to a required tolerance.

The shell element is obtained from the three-dimensional solid element by imposing two constraints: 1) straight lines normal to the midsurface before deformation remain straight but not normal after deformation; and 2) the transverse normal components of strain and, hence, stress are ignored in the development. These assumptions degenerate a three-dimensional theory to a two-dimensional theory, and the resulting shell element is called three-dimensional degenerated shell element. The nonlinear formulation admits large displacements and rotations of the shell element and small strains since the thickness does not change and the normal does not distort.

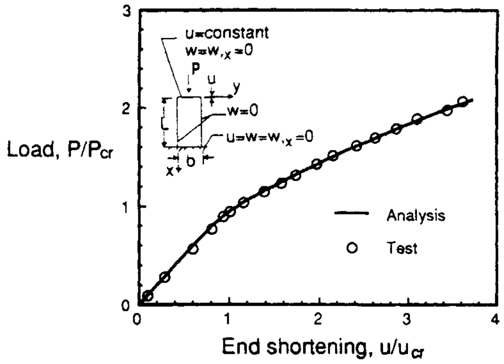

a) End shortening

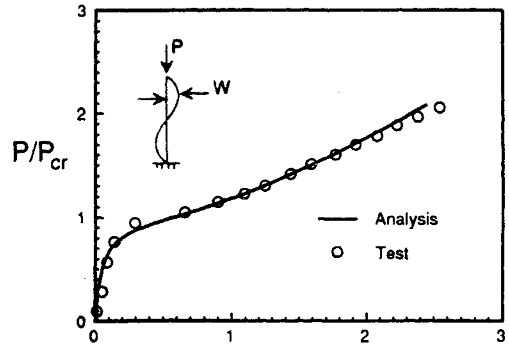

b) Out-of-plane deflection

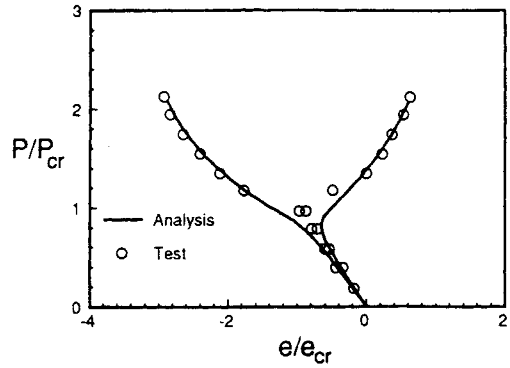

c) Surface strains

**Fig. 3 Postbuckling response characteristics: specimen C4.**

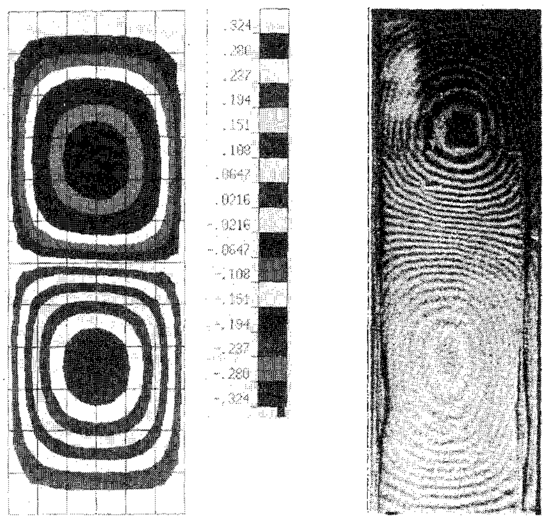

**a) Contour plot of analytical results**

**b) Photograph of moire-fringe pattern (from Ref. 4)**

**Fig. 4 Comparison of experimental and analytical out-of-plane deflection patterns: specimen C4.**

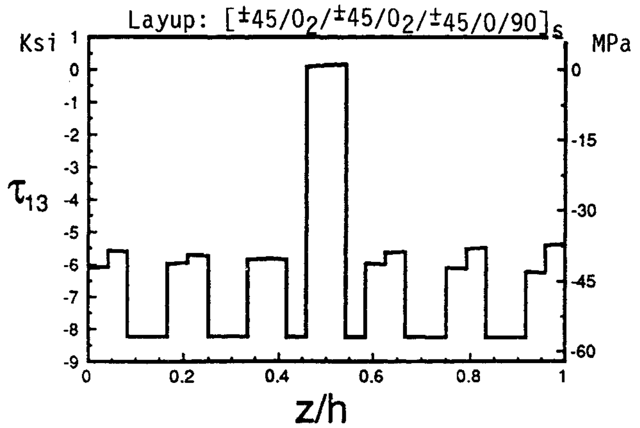

**Fig. 5 Transverse shear $\tau_{13}$ distributions through the thickness: specimen C4.**

In the process of evaluating the integrals in Eq. (1) (e.g., $[K_L]$, $[K_{\mathrm{NL}}]$, $\{F\}$), Gauss quadrature is used in the membrane directions of the shell, but explicit integration is used in the thickness direction. Thus, the thickness direction integration for all three matrices reduces to the following classical laminate stiffnesses,

$$[A] = \sum_{k=1}^{P} [C']_k(\zeta_{k+1} - \zeta_k)$$

$$[B] = \frac{1}{2}\sum_{k=1}^{P} [C']_k(\zeta_{k+1}^2 - \zeta_k^2) \tag{3}$$

$$[D] = \frac{1}{3}\sum_{k=1}^{P} [C']_k(\zeta_{k+1}^3 - \zeta_k^3)$$

where $\zeta_k$ is the thickness coordinate of the bottom of the $k$th lamina, $P$ the number of laminas, and $[C']$ the constitutive matrix for the $k$th lamina in the principal material coordinates. The transformations for $[C']$ can be found in Ref. 5, but in functional form it can be stated as

$$[C'] = f([Q],\theta) \tag{4}$$

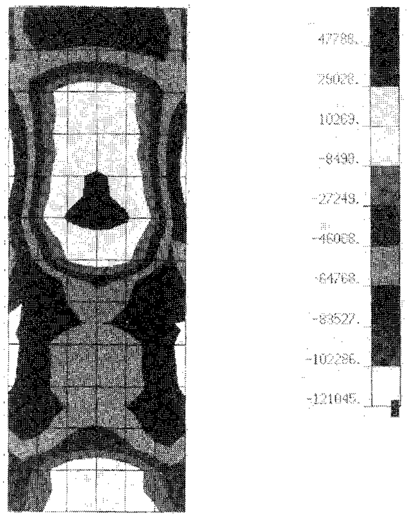

**a) Contour plot of axial stress distributions**

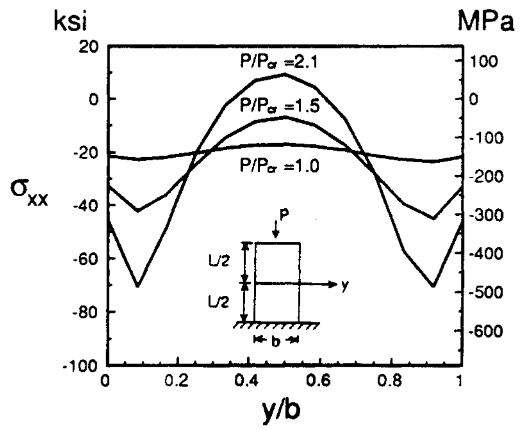

**b) Stress distributions across panel midlength**

**Fig. 6 Axial stress $\sigma_{xx}$ distributions in the third layer (0-deg ply) from the surface.**

where $Q_{ij}$ are the plane stress-reduced elastic coefficients in the material coordinates, and $\theta$ is the fiber orientation angle. For an orthotropic lamina, $Q_{ij}$ can be expressed as

$$Q_{11} = \frac{E_{11}}{1 - \nu_{12}\nu_{21}}, \quad Q_{12} = \frac{\nu_{12}E_2}{1 - \nu_{12}\nu_{21}}, \quad Q_{22} = \frac{E_{22}}{1 - \nu_{12}\nu_{21}}$$
$$Q_{44} = (G_{13})_R, \quad Q_{55} = (G_{23})_R, \quad Q_{66} = G_{12} \tag{5}$$

where $E_{11}$, $\nu_{12}$, $\nu_{21}$, $E_{22}$, $G_{13}$, $G_{23}$, $G_{12}$ are the engineering lamina properties, and $k$ is the shear correction taken to be 5/6.

## Failure Analysis

### Failure Criteria

Two failure criteria are investigated in this work: the maximum stress and the Tsai-Wu criteria. Both are single-point phenomenological theories used to predict first-ply failure. Any other closed-form criteria could have been used, including strain-based criteria. The two criteria used are described below (see Ref. 7).

*Maximum Stress Criterion*

Failure occurs if any one of the following conditions are satisfied:

$$X_c > \sigma_1 > X_t, \qquad \sigma_4 > R$$
$$Y_c > \sigma_2 > Y_t, \qquad \sigma_5 > S, \qquad \sigma_6 > T \tag{6}$$

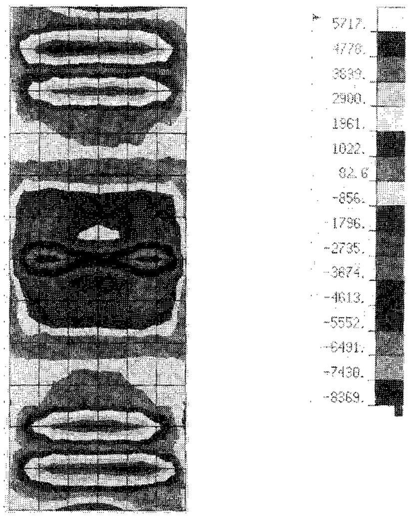

**a) Contour plot of transverse shear-stress distributions**

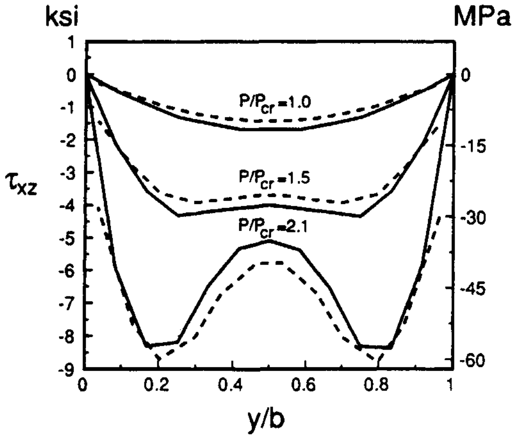

**b) Stress distributions across panel midlength**

**Fig. 7 Transverse shear-stress $\tau_{xz}$ distributions in the third layer (0-deg ply) from the surface: specimen C4.**

where $\sigma_1$, $\sigma_2$ are normal stresses along the fiber and normal to the fiber, respectively, and $\sigma_4$, $\sigma_5$, $\sigma_6$ are the shear stresses in the 23, 13, and 12 planes, respectively; $X$ and $Y$ correspond to the strengths in the 1 and 2 directions, and the subscripts $t$ and $c$ denote tension and compression, respectively; $R$, $S$, and $T$ are the shear strengths in the 23, 13, and 12 planes, respectively.

*Tsai-Wu Criterion*

Failure occurs if the following single condition is satisfied:

$$F_1\sigma_1 + F_2\sigma_2 + 2F_{12}\sigma_1\sigma_2 + F_{11}\sigma_1^2 + F_{22}\sigma_2^2 + F_{44}\sigma_4^2 + F_{55}\sigma_5^2 + F_{66}\sigma_6^2 \geq 1 \tag{7a}$$

where

$$F_1 = \frac{1}{X_t} - \frac{1}{X_c}, \quad F_2 = \frac{1}{Y_t} - \frac{1}{Y_c}$$
$$F_{11} = \frac{1}{X_tX_c}, \quad F_{22} = \frac{1}{Y_tY_c}, \quad F_{44} = \frac{1}{R^2},$$
$$F_{55} = \frac{1}{S^2}, \quad F_{66} = \frac{1}{T^2} \tag{7b}$$
$$F_{12} = -\frac{1}{2}\sqrt{\frac{1}{X_tX_cY_tY_c}}$$

### Progressive Failure

It is well known that true failure of a laminated composite panel does not occur at the load corresponding to the first-ply failure. In reality, failure occurs due to propagation of failures (or damage) as the load is increased. To model this effect, an analytical progressive failure technique is included in the nonlinear analysis. At each load step, Gauss point stresses were used in the selected failure criterion. If failure occurred at a Gauss point, a reduction in lamina stiffness was applied to that point, which changed the resultant *A-B-D* laminate stiffnesses of Eqs. (3). For example, for the maximum stress criterion, if the $\sigma_1$ stress exceeds the longitudinal tensile strength $X_t$, then the longitudinal modulus $E_{11}$ at that point is reduced to zero. For the case of the Tsai-Wu criterion, if failure occurs, then the following terms were used to determine the failure mode:

$$
\begin{gathered}
H_1 = F_1\sigma_1 + F_{11}\sigma_1^2 \\
H_2 = F_2\sigma_2 + F_{22}\sigma_2^2 \qquad (8) \\
H_4 = F_{44}\sigma_4^2, \quad H_5 = F_{55}\sigma_5^2, \quad H_6 = F_{66}\sigma_6^2
\end{gathered}
$$

The largest $H_i$ term was selected to be the dominant failure mode and the corresponding moduli was reduced to zero. $H_1$ corresponds to the modulus $E_{11}$, $H_2$ to $E_{22}$, $H_4$ to $G_{23}$, $H_5$ to $G_{13}$, and $H_6$ to $G_{23}$. A consequence of this reduction is a requirement to store updated (or damaged) engineering material properties as the failure progresses. An outline of the steps required is given in the following:

1) After nonlinear iterative convergence is achieved, calculate stresses at the middle of each layer at each Gauss point.
2) Transform to principal stresses.
3) Compute failure indices.
4) If failure occurs, reduce the appropriate lamina moduli at that Gauss point, recompute laminate stiffnesses, and restart nonlinear analysis at the same load step.
5) If no failure occurs, proceed to next load step.

To determine the final failure, the analytical end-shortening results were monitored as in a compression test. The failure load is defined to be that load for which large changes in end shortening occur for small changes in load. This is indicated by sharp changes in the load vs end-shortening curves, such that the slope of the load-deflection curve becomes very small (see Figs. 8, 11, and 14). For this work, a qualitative judgement of the failure load was made by inspecting the load-deflection curve for a sharp change in slope.

## Results of C4 Panel

Comparison between test results from Ref. 4 and finite element results from Ref. 6 for panel C4 are shown in Fig. 3. End shortening $u$ normalized by the analytical end shortening $u_{cr}$ at buckling (Fig. 3a), out-of-plane deflection $w$ near a point of maximum deflection normalized by the panel thickness $t$ (Fig. 3b), and the longitudinal surface strains $e$ near a point of maximum out-of-plane deflection normalized by the analytical buckling strain $e_{cr}$ (Fig. 3c) are shown as a function of the applied load $P$ normalized by the analytical buckling load $P_{cr}$. The circles in the figure represent test data, and the curves represent analytical data determined from nonlinear finite element analyses. These experimental and analytical results correlate well up to failure of the panel. The postbuckling response exhibits large out-of-plane deflections (nearly three times the panel thickness, see Fig. 3b) and high-longitudinal surface strains (nearly three times the analytical buckling strain, see Fig. 3c). In addition, this panel was also analyzed in Ref. 6 using two other finite element formulations, one of which utilized the classical laminated plate theory with the

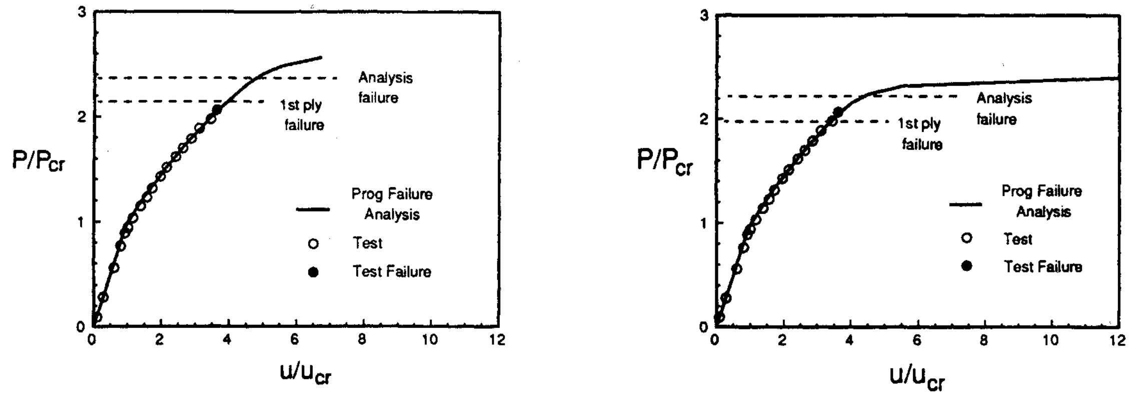

a) Maximum stress failure criterion b) Tsai-Wu failure criterion

Fig. 8 Progressive failure results: specimen C4.

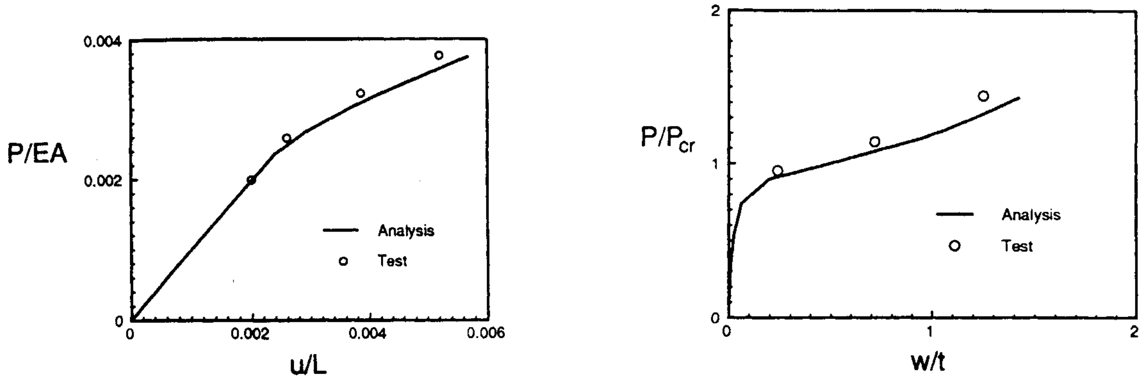

a) End shortening b) Out-of-plane deflection

Fig. 9 Postbuckling response characteristics: specimen C10.

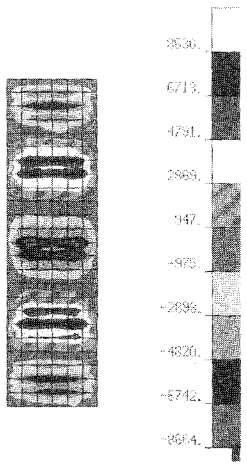

a) Contour plot of transverse shear-stress distributions

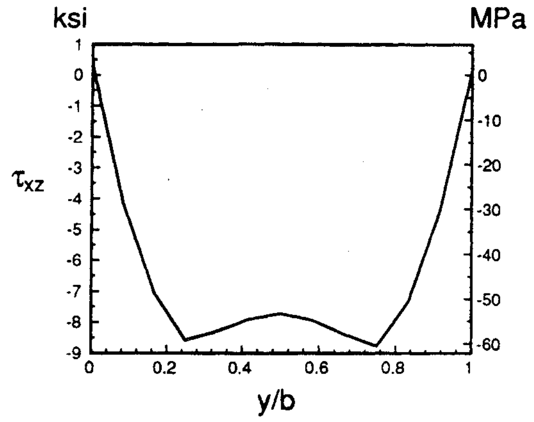

b) Stress distributions across panel midlength

**Fig. 10 Transverse shear-stress $\tau_{xz}$ distributions in layer 22 (0-deg ply) from the surface: specimen C10.**

effects of transverse shear neglected. In that work, it was concluded that the presence of shear flexibility improved the element convergence characteristics, particularly when operating deep in the postbuckling regime.

A contour plot of the out-of-plane deflections generated from the nonlinear analysis using the Chao-Reddy nine-node element at an applied load of 2.1 $P_{cr}$ is shown in Fig. 4a. A photograph of the moire-fringe pattern from Ref. 4 and corresponding to the out-of-plane deflections observed during the testing of panel C4 at the same load is shown in Fig. 4b. These results indicate that the out-of-plane deflections from both test and analysis have the same shape over the entire panel. Both patterns indicate two longitudinal half-waves with a buckling-mode nodal line at panel midlength.

Stress distributions in each layer of the laminate were analytically evaluated using the nonlinear results obtained with the 9CR model in order to determine analytically the failure loads. The stresses were determined using the constitutive relations for both the in-plane and transverse components. In addition, the transverse shear-stress distributions were obtained by integrating the equilibrium equations and using the in-plane stresses obtained using the constitutive relations. The distribution of the peak $\tau_{13}$ stress through the thickness direction normalized by the laminate thickness $h$ is shown in Fig. 5, indicating that the 0-deg layers carry the highest transverse shear load. Through these analyses, the third layer in the laminate (a 0-deg ply) was found to have the highest overall stresses. Examination of these stress distributions and their redistribution after the panel buckles provides insight into the failure characteristics of these panels.

The distribution over the entire panel of the axial stress $\sigma_{xx}$ in the third layer of the laminate (a 0-deg ply) is shown in Fig. 6a at an applied load of 2.1 $P_{cr}$. This distribution indicates that high compressive axial stresses occur along the longitudinal edges of the panel. The redistribution of the axial stress in this 0-deg ply at panel midlength is indicated in Fig. 6b for three values of the applied load. The $y$ coordinate across the panel is measured from the left side and normalized by the panel width $b$. Near the buckling load, the axial stress is nearly uniform across the panel. After buckling, the longitudinal membrane strain in the vicinity of the buckling mode crests is relieved by the large deflections associated with panel buckling and redistributed toward the edges of the panel. The peaks do not occur right at the edges because the $\psi_x$ rotation is enforced to be zero due to the knife edge supports, thus decreasing the magnitude of both the linear and nonlinear terms of the longitudinal strain $\epsilon_{xx}$. Although the axial stress is large, the values are well below the material allowable values [1400 MPa (203 ksi) in tension; 1138 MPa (165 ksi) in compression].

The distribution over the entire panel of the transverse shear stress $\tau_{xz}$ in the third layer of the laminate (a 0-deg ply) is shown in Fig. 7a at an applied load of 2.1 $P_{cr}$. This distribution indicates that high transverse shear stresses occur along the buckling-mode nodal line. The redistribution of this transverse shear stress in this 0-deg ply at panel midlength is indicated in Fig. 7b for three values of the applied load. The solid curves represent the transverse shear-stress distributions obtained using the constitutive relations and the transverse shearing strain distribution. The dashed curves represent the transverse shearing stress distributions obtained by integrating the local equilibrium equations of each lamina. These solid curve distributions are very similar to those obtained using the equilibrium equations (the dashed curves), the latter believed to be more accurate. Near the buckling load, the peak transverse shear stress occurs near the center of the panel. After buckling, the transverse shear stresses ($\tau_{xz}$) redistribute toward the edges of the panel. The peak values of the transverse shear

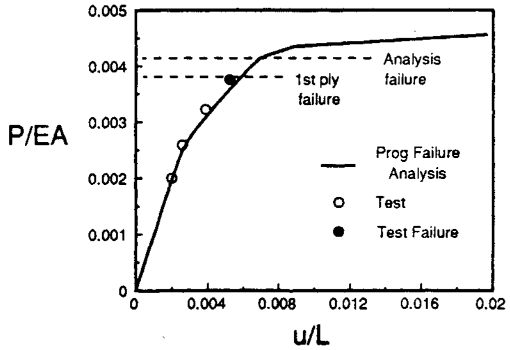

a) Maximum stress failure criterion

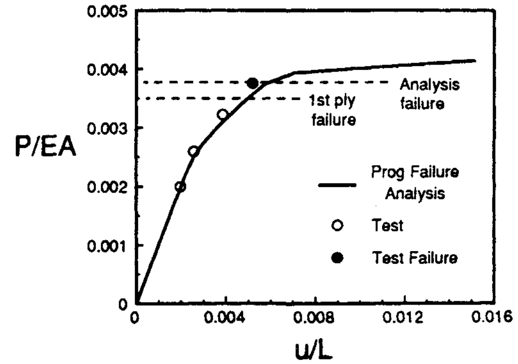

b) Tsai-Wu failure criterion

**Fig. 11 Progressive failure results: specimen C10.**

stress $\tau_{xz}$ approaches the material allowable value [62 MPa (9ksi)]. In addition, it should be mentioned that the transverse shear stresses can be recovered for this relatively thin panel by integrating the local equilibrium equations of a classical plate theory, as well as the shear deformation theory used earlier; however, it is believed that the latter is more accurate due to the conclusions discussed previously from Ref. 6.

Close examination of the Green-Lagrange strain component $\epsilon_{xz}$ given by

$$\epsilon_{xz} = \frac{1}{2}\left[\frac{\partial u}{\partial z} + \frac{\partial w}{\partial x} + \frac{\partial u}{\partial x}\frac{\partial u}{\partial z} + \frac{\partial v}{\partial x}\frac{\partial v}{\partial z} + \frac{\partial w}{\partial x}\frac{\partial w}{\partial z}\right] \tag{9}$$

in conjunction with the displacement field of the first-order shear deformation theory

$$u(x,y,z) = u_0(x,y) + z\psi_x, \quad v(x,y,z) = v_0(x,y) + z\psi_y$$

$$w(x,y,z) = w_0(x,y) \tag{10}$$

provides additional insight useful in characterizing the failure mode. Substituting Eqs. (10) into Eq. (9) and noting that, along a buckling-mode nodal line $\psi_y$, $\partial w/\partial y$, and $\partial \psi_x/\partial x$ are small and $\partial w/\partial x$ is large, gives

$$\epsilon_{xz} = \frac{1}{2}\left[\frac{\partial w_0}{\partial x} + \psi_x + \frac{\partial u_0}{\partial x}\psi_x\right] \tag{11}$$

The quantity $\partial w_0/\partial x$ (out-of-plane deflection gradient) is largest along a buckling-mode nodal line, and the quantity $\partial u_0/\partial x$ (related to the membrane strain) is largest along the panel edges. Examination of the other transverse shearing strain $\epsilon_{yz}$ in a similar manner leads to the conclusion that the transverse shearing strain $\epsilon_{xz}$ is the dominant one.

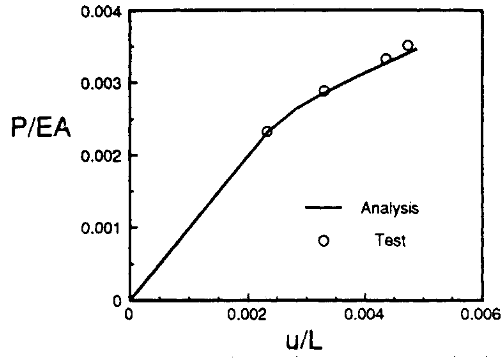

a) End shortening

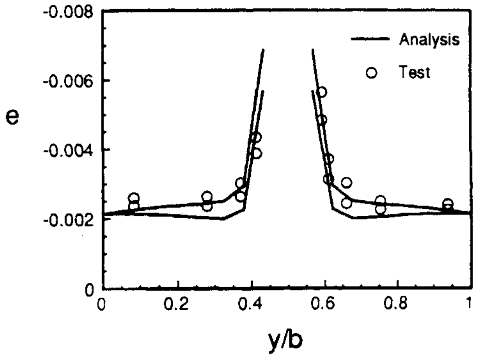

b) Surface strains at $P/P_{cr} = 0.90$

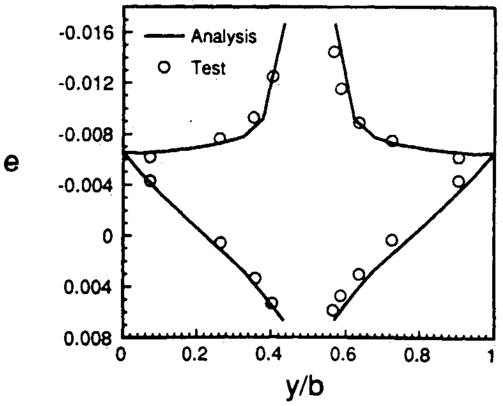

c) Surface strains at $P/P_{cr} = 1.39$

Fig. 12 Postbuckling response characteristics; specimen H4.

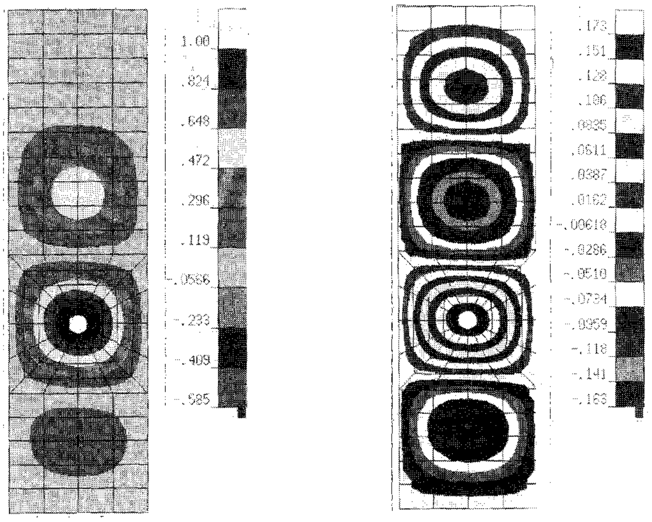

a) Linear buckling mode 1

b) Postbuckling mode at $P/P_{cr} = 1.39$

Fig. 13 Analytical out-of-plane deflection patterns: specimen H4.

Based on the finite element analysis results and an intuitive examination of the Green-Lagrange strain components along a buckling-mode nodal line, the failure mode of panel C4 is attributed to large transverse shearing stresses. This result is consistent with and substantiates the observations of Starnes and Rouse in Ref. 4.

The progressive failure results for panel C4 are presented in Figs. 8a and 8b using the maximum stress and Tsai-Wu failure criteria, respectively. The analytical and experimental end-shortening results are repeated as an aid, and the solid lines are the progressive failure results. In addition to the strengths already mentioned, the other allowables are as follows: transverse tensile strength of 80.9 MPa (11.7 ksi), transverse compressive strength of 189.0 MPa (27.4 ksi), and in-plane shear strength of 69.0 MPa (10.0 ksi). At some point in the analysis, a dramatic change in slope indicates an inability to support additional load. This location is marked as the analytical failure load, and the final experimental data point is the experimental failure load. Comparing curves 8a and 8b, the Tsai-Wu criterion more closely estimates the experimental failure. This is attributed to the interaction effect of the stresses present in the Tsai-Wu criterion's failure index, so that the initial (first-ply) failures tend to be earlier than that of the maximum stress criterion.

## Results of C10 Panel

Analytical and experimental comparisons for end shortening $u$ and out-of-plane deflection $w$ are shown in Figs. 9a and 9b. In these figures, $E$ is the laminate longitudinal modulus, $A$ the cross-sectional area, and $L$ the specimen length. Agreement is not as good as in the C4 specimen because extracting non-normalized experimental data from Ref. 4 was more diffi-

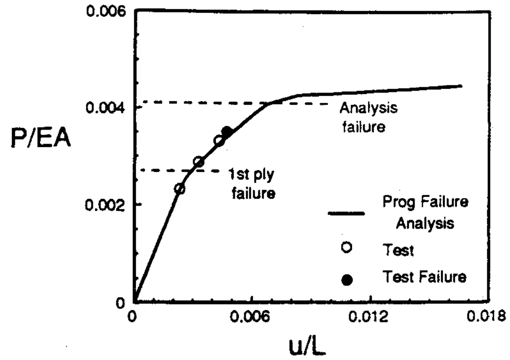

a) **Maximum stress failure criterion**

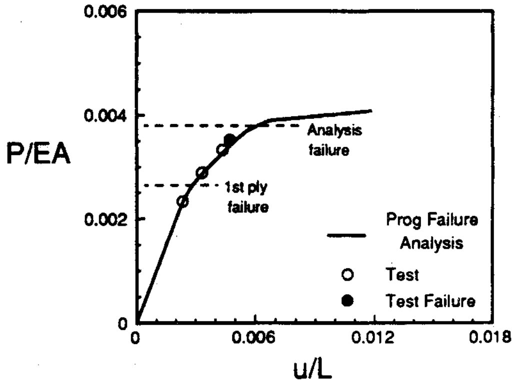

b) **Tsai-Wu failure criterion**

**Fig. 14 Progressive failure results: specimen H4.**

cult. From a linear buckling analysis it was learned that the first mode has three longitudinal half-waves and the second mode has four longitudinal half-waves. The moire-fringe results from Ref. 4 in the postbuckling range exhibited four half-waves. Thus, a linear combination of 1.5% panel thickness of mode 1 and 1.5% panel thickness of mode 2 was used to assist in the change that occurs at the critical buckling load from the three half-wave to the four half-wave mode.

A transverse shear failure mechanism develops for this panel, similar to panel C4. Each nodal line in the buckling mode develops the high-transverse shear stresses, with the peak at the midlength of the panel. Figure 10a shows the distribution of $\tau_{xz}$ in layer 22 (a 0-deg ply), where the three peak $\tau_{xz}$ nodal line concentrations can be seen. Figure 10b contains the familiar $\tau_{xz}$ distribution at the experimental failure load ($1.44P_{\mathrm{cr}}$) across the panel width. The results are similar to those obtained for panel C4.

The progressive failure results for panel C10 are shown in Figs. 11a and 11b. For this panel, the Tsai-Wu criterion correlated extremely well with the experimental results. However, as seen previously for panel C4, the maximum stress criterion did not agree as well.

## Results of H4 Panel

The H4 specimen was analyzed to investigate analytical predictions of deformation and failure for a specimen with a hole. Figure 12a contains end-shortening analytical and experimental comparisons. Figures 12b and 12c show the longitudinal surface strains $e$ (both top and bottom surfaces) across the panel at the hole for a load of $0.90P_{\mathrm{cr}}$ and $1.39P_{\mathrm{cr}}$, respectively. These results are in good agreement with experimental results from Ref. 4. Linear buckling (mode 1) and postbuckling out-of-plane deflection mode shapes for this panel are shown in Figs. 13a and 13b. An imperfection of 1% of panel thickness for mode 1 was used to proceed into the postbuckling range. One can see that four longitudinal half-waves develop in the postbuckled range.

An important note for analysts is that, if uniformly reduced or selective reduced integration was used in the analysis of this panel, spurious modes developed due to zero energy modes and lack of restraint of the model around the hole, which polluted the nonlinear results. Element distortion around the hole could be another contributing factor. It was necessary to use full integration to alleviate this problem, and the mesh had to be sufficiently refined so that locking effects were negligible.

For the H4 panel, the familiar transverse shear mechanism develops along nodal lines away from the hole. However, the peak stress approaches 48.3 MPa (7.0 ksi) at the experimental failure load. The in-plane shear stress was more closely approaching its allowable around the hole at this load. It turns out that simultaneous first-ply failure due to $\tau_{12}$ and $\sigma_1$ components around the hole edge occurs. Thus, the failure mode was not a dominant transverse shear mode as in the previous panels, but a more complex interacting mode with a dominant in-plane shear component. Progressive failure results are shown in Figures 14a and 14b. The Tsai-Wu criterion was in good agreement with experimental results and was much better than the maximum stress criterion.

## Concluding Remarks

The postbuckling response and failure modes of graphite-epoxy panels with and without holes loaded in axial compression have been studied. Good correlation between the experimentally obtained and analytically predicted postbuckling responses were obtained. Analytical predictions of the failure mode and location agreed well with those obtained in Ref. 4. A progressive failure technique is described and used to predict total failure of the panels with good results as compared to the experimental results in Ref. 4. The inclusion of shear deformation improves the element convergence characteristics as discussed in Ref. 6.

## Acknowledgments

The work of the first and second authors was supported in part by NASA Grants NAG-1-1030 and NAG-1-1085. The work of the third author was performed while employed by NASA Langley Research Center.

## References

[1]Noor, A. K., and Burton, W. S., "Assessment of Shear Deformation Theories for Multilayered Composite Plates," *Applied Mechanics Reviews,* Vol. 42, No. 1, 1989, pp. 1-13.

[2]Reddy, J. N., "On Refined Computational Models of Composite Laminates," *International Journal for Numerical Methods in Engineering,* Vol. 27, No. 2, 1989, pp. 361-382.

[3]Reddy, J. N., "A Review of Refined Theories of Laminated Composite Plates," *Shock and Vibration Digest,* Vol. 22, No. 7, 1990, pp. 3-17.

[4]Starnes, J. H., Jr., and Rouse, M., "Postbuckling and Failure Characteristics of Selected Flat Rectangular Graphite-Epoxy Plates Loaded in Compression," AIAA Paper 81-0543, April 1981.

[5]Chao, W. C., and Reddy, J. N., "Analysis of Laminated Composite Shells Using a Degenerated 3-D Element," *International Journal for Numerical Methods in Engineering,* Vol. 20, No. 11, 1984, pp. 1991-2007.

[6]Engelstad, S. P., Knight, N. F., Jr., and Reddy, J. N., "Interlaminar Shear Stress Effects on the Postbuckling Response of Graphite-Epoxy Panels," NASA TM-102626, April 1990.

[7]Reddy, J. N., and Pandey, A. J., "A First-Ply Failure Analysis of Composite Laminates," *Computers and Structures,* Vol. 25, No. 3, 1987, pp. 371-393.